IOP PUBLISHING PHYSICS IN MEDICINE AND BIOLOGY

Phys. Med. Biol. **52** (2007) 4863–4880 doi:10.1088/0031-9155/52/16/010

Experimental evaluation of fiber-interspaced antiscatter grids for large patient imaging with digital x-ray systems

Kenneth A Fetterly and Beth A Schueler

Mayo Clinic, 200 1st St SW, Rochester, MN 55905, USA

Received 5 January 2007, in final form 22 June 2007
Published 30 July 2007
Online at stacks.iop.org/PMB/52/4863

Abstract

Radiographic imaging of large patients is compromised by x-ray scatter. Optimization of digital x-ray imaging systems used for projection radiography requires the use of the best possible antiscatter grid. The performance of antiscatter grids used in conjunction with digital x-ray imaging systems can be characterized through measurement of the signal-to-noise ratio (SNR) improvement factor (K_{SNR}). The SNR improvement factor of several linear, focused antiscatter grids was determined from measurements of the fundamental primary and scatter transmission fraction measurements of the grids as well as the inherent scatter-to-primary ratio (SPR) of the x-ray beam and scatter phantom. The inherent SPR and scatter transmission fraction was measured using a graduated lead beam stop method. The K_{SNR} of eight grids with line rates (N) in the range 40 to 80 cm^{-1} and ratios (r) in the range 8:1 to 15:1 was measured. All of the grids had fiber interspace material and carbon-fiber covers. The scatter phantom used was Solid Water® with thickness 10 to 50 cm, and a 30 × 30 cm^2 field of view was used. All measurements were acquired using a 104 kVp x-ray beam. The SPR of the non-grid imaging condition ranged from 2.55 for the 10 cm phantom to 25.9 for the 50 cm phantom. The scatter transmission fractions ranged from a low of 0.083 for the N50 r15 grid to a high of 0.22 for the N40 r8 grid and the primary transmission fractions ranged from a low of 0.69 for the N80 r15 grid to 0.76 for the N40 r8 grid. The SNR improvement factors ranged from 1.2 for the 10 cm phantom and N40 r8 grid to 2.09 for the 50 cm phantom and the best performing N50 r15, N44 r15 and N40 r14 grids.

1. Introduction

X-ray attenuation by patient tissue is a combination of x-ray energy absorption and x-ray scatter. In projection x-ray imaging, scattered x-rays may exit the tissue and contribute

unwanted energy to the x-ray image. The scattered x-ray energy constitutes a source of x-ray noise, thereby compromising image quality. Methods used to control the amount of scatter reaching an imaging detector include the use of an air gap, slot scanning geometry, focused linear grids and other antiscatter grid configurations. Of these, use of a focused linear grid is the method commonly used to minimize the detrimental effects of x-ray scatter in projection x-ray imaging systems.

That control of x-ray scatter using antiscatter grids is beneficial to x-ray projection imaging has been known for quite some time. Gustav Bucky described the first scatter control device for x-ray imaging in 1913 (Bucky 1913). The interested reader is encouraged to review a series of papers by Bonenkamp and Boldingh for a thorough description of the design and implementation challenges of focused linear grids (Bonenkamp and Boldingh 1959a, 1959b, 1959c, Boldingh 1962). For screen–film (SF) imaging, the image quality benefit achieved through grid use is commonly described as the contrast improvement factor (K_C) (Bonenkamp and Boldingh 1959a, Morgan 1946). The mechanism of image quality improvement via the contrast improvement factor is known. A screen–film system requires a fixed total exposure to ensure proper film darkening. The total exposure is a combination of primary x-ray photons, which carry anatomical information, and scattered photons. The grid preferentially attenuates a large fraction of the scattered photons compared to a small fraction of the primary photons. Thus, an image acquired with a grid has a greater fraction of primary photons, resulting in an improved anatomical and radiographic image contrast. For screen–film imaging, the benefit of improved anatomical contrast comes at a cost. Because the grid attenuates a large fraction of the total x-ray energy directed toward the screen–film detector, the x-ray technique (mA s and/or kVp) has to be increased to ensure proper film darkening. The Bucky factor (B) is the multiplicative factor by which the x-ray technique must be increased to ensure that the same total exposure is realized by the detector, thus ensuring appropriate film optical density (Bucky 1913, Bonenkamp and Boldingh 1959a, Wilsey 1921). Grids with relatively high contrast improvement factors also have high Bucky factors. In SF imaging, selection of an appropriate grid for clinical use is generally a compromise between achieving the desired image quality improvements (K_C) and maintaining an acceptably low Bucky factor.

Digital x-ray imaging devices have a linear (or log-linear) response to exposure. Unlike screen–film imaging, digital imaging devices are not restricted to a fixed total exposure because the final grayscale rendition of digital images is controlled by image processing. Because digital systems do not have a fixed total exposure requirement, the screen–film Bucky factor is not relevant, and an antiscatter grid can improve image quality independent of changes to the x-ray technique. The image quality benefits of antiscatter grid use with a digital imaging system are best described by the quantum signal-to-noise ratio (SNR) improvement factor (K_{SNR}) (Dick and Motz 1978, Neitzel 1992). The SNR improvement factor defines the relative change in the quantum SNR of an image obtained with a grid versus a (otherwise similar) non-grid technique. From the perspective of digital x-ray system optimization, changes in the square of the SNR improvement factor associated with a grid can be considered equivalent to changes in the detective quantum efficiency of the x-ray detector.

As was the case in screen–film imaging, acquiring quality x-ray images of large patient anatomy remains a challenge for digital x-ray imaging systems due to significant attenuation of primary x-rays and a relatively large contribution of x-ray scatter to the image. That computed radiography is more sensitive to x-ray scatter than the screen–film is known (Floyd *et al* 1991, Tucker *et al* 1993, Yip *et al* 1996). Investigation of the sensitivity of the various flat panel x-ray imaging technologies is warranted. It has long been known that the inherent useful information content of an x-ray beam can be improved simply by the addition of a proper antiscatter grid (Motz and Danos 1978). The mathematical theories describing the benefit of antiscatter grids

in a digital imaging environment have been presented in previous works by others (Dick and Motz 1978, Neitzel 1992, Motz and Danos 1978, Chan *et al* 1985, Wagner 1977, Wagner *et al* 1980). Published investigations of the influence of grid use with digital radiography systems have included experimental (McDaniel *et al* 1984, Chan *et al* 1990, Sandborg *et al* 1994), Monte Carlo (Kalender 1982, Chan *et al* 1990, Sandborg *et al* 1994) and other model (Motz and Danos 1978, Neitzel 1992) studies. With limited exception (Sandborg *et al* 1994), these works investigated the influence of Al (or unspecified) interspaced grids, and there remains a general lack of information available regarding the performance of commercially available fiber-interspaced grids to guide effective design and clinical use of digital imaging systems.

The purpose of this work is to evaluate the image quality improvements that might be expected from a select group of commercially available fiber-interspaced grids. This work will measure the SNR improvement factor of these grids using a wide range of x-ray scatter conditions, but was designed specifically to investigate the influence of grid use for large patients. To accommodate the desire to investigate grids specifically for large patients, measurements were performed using a nominal 100 kVp x-ray beam. For this work, x-ray beam and grid alignment were carefully controlled. The influence of misalignment on grid performance has been presented by others (Boldingh 1962, Carlin *et al* 1996) and will not be specifically addressed in this work. The potential for stationary grids to produce image artifacts when used with a digital detector will also not be specifically addressed in this work.

2. Theory

The general theory of assessing digital image quality improvement using the SNR improvement factor (and similar precursors) has been presented by other authors (Wagner 1977, Dick and Motz 1978, Motz and Danos 1978, McDaniel *et al* 1984, Chan *et al* 1990, Neitzel 1992, Sandborg *et al* 1994). For this work, it will be assumed that the noise properties of the digital x-ray imaging system are quantum limited. There are two fundamental grid characteristics which serve to define grid performance, the fraction of the primary (T_P) and scattered x-ray signal (T_S) that is transmitted by the grid (Bonenkamp and Boldingh 1959a, Dick and Motz 1978). If the scatter-to-primary ratio (SPR) of an x-ray beam is known, then the SNR improvement factor (K_{SNR}) associated with a particular grid can be directly calculated. The appendix provides a derivation of K_{SNR} using these three terms as

$$K_{SNR} = \frac{(1 + SPR)^{0.5} T_P}{(T_P + T_S SPR)^{0.5}}. \tag{1}$$

Note that the potential for increased K_{SNR} increases with increased SPR.

While this work will use equation (1) to define K_{SNR}, there are other definitions that may be of interest. Because they are well known, widely reported in the literature, and readily measurable quantities, it was desirable to define K_{SNR} in terms of the scatter-to-primary ratio of the x-ray beam incident upon the x-ray detector for both the non-grid (SPR) and grid (SPR_G) imagining conditions and the Bucky factor. Derivation of K_{SNR} using these three quantities is provided in the appendix, and results in the SNR improvement factor defined as

$$K_{SNR} = \frac{(1 + SPR)}{B^{0.5}(1 + SPR_G)}. \tag{2}$$

Note that substituting the definition of the contrast improvement factor (K_C),

$$K_C = \frac{(1 + SPR)}{(1 + SPR_G)}, \tag{3}$$

into equation (2) results in

$$K_{SNR} = \frac{K_C}{B^{0.5}}. \tag{4}$$

K_{SNR} as defined in equation (4) may be useful to determine an equivalent K_{SNR} from published works that report K_C and B (Doi *et al* 1983, Chan *et al* 1985). Other authors have reported the scatter fractions with and without a grid (McDaniel *et al* 1984). Equation (3) may be readily modified to define K_{SNR} as a function of scatter fractions rather than the scatter-to-primary ratio.

3. Materials and methods

The general structure of a focused linear grid is well known, and details are available in several references. Following the nomenclature of Bonenkamp and Boldingh (1959a) and IEC 60627—'Diagnostic X-ray imaging equipment—characteristics of general purpose and mammographic antiscatter grids' (IEC 2001), the grid ratio (r) is defined as

$$r = \frac{h}{D}, \tag{5}$$

where h is the height of the lead septa, and D is the distance between adjacent lead septa (interspace). The lead strip frequency, or line rate (N), of the grid is specified as

$$N = \frac{1}{(D+d)}, \tag{6}$$

where d is the thickness of the lead septa, and N is usually specified with units of cm^{-1}. The focal distance (f_0) of a focused linear grid is specified with units of cm.

The SNR improvement factor was measured for two series of four focused linear grids each. One series had a constant line rate of $N = 40\ cm^{-1}$ and grid ratios 8:1, 10:1, 12:1 and 14:1. The other series had a constant ratio of $r = 15{:}1$ with line rates of 44, 50, 60 and 80 cm^{-1}. The grids (Smit Roentgen, The Netherlands) had lead septa, fiber interspace material and carbon fiber covers. The lead septa thickness of the grids was 36 μm, except the 15:1, 80 cm^{-1} grid had 27.5 μm thick septa. The focal distance of the grids was 100 cm. The grids were installed into a portable Bucky mechanism for the imaging experiments. As will be discussed in more detail later, the Bucky mechanism was held fixed when measuring T_P and put into motion when measuring T_S.

The Solid Water® scatter phantom used had a cross-sectional area of 30 × 30 cm^2 and ranged in thickness from 10 to 50 cm in 10 cm increments. The phantom was positioned such that the exit surface of the phantom remained in contact with the entrance surface of the Bucky mechanism used to contain the grids and the computed radiography storage phosphor cassette x-ray detector used for these experiments. The raw x-ray beam used for this was created using a standard x-ray tube with a tungsten target and 104 kVp. This peak tube potential was found to provide characteristics consistent with a RQA8 beam (34 mm type 1100 Al filtration, 9.9 mm type 1100 Al half value layer). Note that the IEC 1267 recommends using a RQN6 beam to characterize x-ray grid performance. The RQN6 beam has an approximate tube voltage of 80 kVp and a 20 cm thick water attenuator phantom. The higher 104 kVp beam was selected for this work because it is similar to that which would be used clinically for thick patient anatomy (greater than 35 cm), and it provided x-ray transmission through the phantom which was sufficient to make measurements without an unreasonable burden on the x-ray tube. Similar to the IEC 1267 report, the x-ray field of view was restricted to 30 × 30 cm^2 at the input surface of the Bucky. The x-ray source to grid distance was fixed to

100 cm. The computed radiography cassette was placed in the Bucky mechanism, immediately beyond the antiscatter grid.

All measurements were acquired using a Fuji computed radiography system as the imaging device (Fuji Medical Systems, Tokyo, Japan). A single model ST-V storage phosphor plate was used, and it was read out in an AC-3 CS-ID reader. The images were read out using the parameters latitude = 4.0 and sensitivity = 200. These settings ensured that the entire dynamic range of the detector system was realized in the output images. For each image acquired, image pixel values were 'linearized' to an equivalent detected x-ray signal using the measured system response function (Floyd *et al* 1991, Flynn and Samei 1999, Fetterly and Hangiandreou 2001). All image data were linearized prior to further analysis. Used in this manner, the CR imaging device may be considered to function as a two-dimensional x-ray signal meter. For a given phantom thickness, the same x-ray technique (current and time) was used for acquiring images with and without the lead beam stops. Preliminary experiments demonstrated that variation in the output of the x-ray tube was less than 2%.

3.1. Scatter-to-primary ratio

The scatter-to-primary ratio of the non-grid (SPR) imaging condition was measured using a graduated beam stop method similar to that presented by Floyd *et al* (1991). Eight lead disks of thickness 3 mm were used. The disks were mounted on a thin sheet of plastic and were always positioned at the point in space that corresponded to the input surface of the 50 cm phantom, or 50 cm from the entrance surface of the Bucky. This positioning ensured that the object magnification of the disks was the same for all phantom thicknesses. The x-ray shadows of the circular beam stops, measured at the image plane, had radii in the range 2.5 mm to 15 mm. The circular pattern of lead disks had a radius of 7 cm at the image plane.

Preliminary experiments demonstrated that CR storage phosphor non-uniformities had the potential to cause relatively large systematic errors. Therefore, a single CR storage phosphor was used and a non-uniformity correction method was implemented. For each phantom thickness, the non-grid SPR was measured from image pairs. One image of the pair had lead beam stops, the other did not. For each pair of images, the location of the center of mass (COM) of each lead beam stop and the radius of the beam stop were determined using semi-automated custom software. For each beam stop, a circular region of interest (ROI) was defined. The center of the ROI corresponded to the COM of the beam stop, and the radius of the ROI was defined as one-half the radius of the beam stop. The average signal of the pixels contained within this ROI was calculated. Given that the eight ROIs were defined to be behind the lead beam stops, these average signal values represent the scatter signal (S_S) contribution to the image containing the lead beam stops. The exact ROI location and size was replicated on the image without the beam stops. Average signal values from these ROIs represent the total image signal (S_T), which is the sum of the scatter and primary x-ray signal (S_P).

Each image pair was acquired using the same x-ray technique (kVp, mA s). However, it is reasonable to expect a small difference in x-ray tube output for repeated exposures. For each image, the x-ray exposure was monitored via sampling of the background exposure signal in the region between beam stops. Eight background exposure ROIs were sampled for each image. The average of the samples from the phantom only image (S_B) and that from the phantom and beams stop image ($S_{B,Pb}$) was calculated. The ratio of these two values,

$$\alpha = \frac{S_B}{S_{B,Pb}}, \tag{7}$$

was used to correct for the modest difference (less than 2%) in x-ray tube output for image pairs.

For each beam stop, the scatter-to-primary ratio was calculated as

$$\mathrm{SPR} = \frac{\alpha S_{\mathrm{S}}}{S_{\mathrm{T}} - \alpha S_{\mathrm{S}}}, \tag{8}$$

where S_{S} is the image signal that is due to scatter only, and S_{T} is the total sum of the scatter and primary x-ray signals. The eight independent SPR values (one for each beam stop) were retained to calculate the SNR improvement factor as a function of beam stop size.

3.2. Scatter transmission

For each grid, the fraction of transmitted scatter was measured using image pairs. One image contained the phantom and lead beam stops and was acquired without a grid and the other image contained the phantom and lead beam stops and was acquired using a grid. The scatter transmission factor was calculated as

$$T_{\mathrm{S}} = \frac{S_{\mathrm{S,G}}}{S_{\mathrm{S}}}, \tag{9}$$

where $S_{\mathrm{S,G}}$ and S_{S} are the exposure signals behind the lead beam stops for the grid and non-grid acquisitions, respectively. For measurement of the scatter transmission, the grids were put into motion using the Bucky mechanism. Compared to using the grids in a stationary configuration, the moving grid is expected to blur grid non-uniformities and thereby help to minimize the potential for associated error.

3.3. Primary transmission

While it is mathematically straightforward to calculate the primary transmission fraction using the two images from which the scatter transmission was measured, preliminary experiments demonstrated that the precision of the primary transmission measurements is compromised by the large fraction of scatter contained in these images. Therefore, the primary transmission was measured using an independent series of scatter-free images.

Precise alignment of the grid with the x-ray beam is required to optimize the primary x-ray transmission. That the grids were positioned 100 cm from the focal spot was verified with a common tape measure. A preliminary experiment was performed to ensure that the grid was properly aligned with the x-ray beam. In this preliminary experiment, the x-ray beam and grid alignment was adjusted until the primary x-ray transmission reached a maximum value. For measurement of the primary transmission, the grids were held in a fixed position to ensure optimum alignment.

For measurement of the primary transmission, only the lead beam stops and the grid were placed between the x-ray source and the CR cassette. The primary transmission was measured using two pairs of images. The images were acquired with and without the lead beam stops and with and without a grid. The images with lead beam stops were used only to position ROIs in the images without lead beam stops. Similar to the methods used to calculate the scatter transmission fraction, the lead beam stops were automatically recognized and the size and location of the beam stops was used to define ROIs on the complimentary image without beam stops. This method ensured that all ROI-based samples used to measure T_{S} and T_{P} were acquired from a similar physical location on the grids and the storage phosphor. Beyond ROI placement, the images with the lead beam stops served no purpose for measurement of the primary transmission. The primary transmission factor was calculated as

$$T_{\mathrm{P}} = \frac{S_{\mathrm{P,G}}}{S_{\mathrm{P}}}, \tag{10}$$

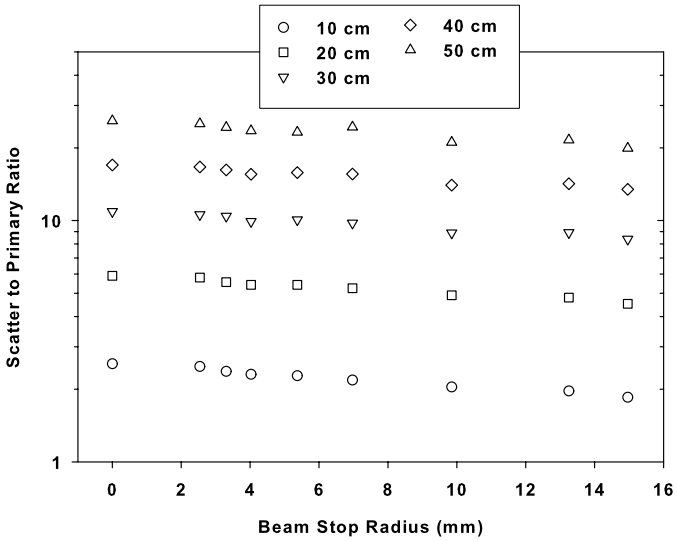

Figure 1. Semi-log plot of the scatter-to-primary ratio as a function of lead beam stop radius measured using Solid Water® phantoms with thickness in the range from 10 to 50 cm. The extrapolated SPR_0 values are provided as the 0 beam stop radius data points.

where $S_{P,G}$ is the primary x-ray signal using the grid, and S_P is the primary absorbed x-ray signal from the non-grid image. T_P was measured at the eight positions in the image which corresponded to the location of the T_S measurement. For each grid, the average of the eight primary transmission fraction measurements was calculated, and only the average value was used in the K_{SNR} definition of equation (1).

3.4. SNR improvement factor

The SNR improvement factor was calculated using the definition provided in equation (1) as well as the SPR, T_S and T_P defined by equations (8), (9) and (10), respectively. K_{SNR} was calculated independently for each of the eight beam stops for each combination of grid and phantom thickness. K_{SNR} was found to be independent of beam stop size. Therefore, the average K_{SNR} value was calculated for each combination of grid and phantom thickness.

4. Results and discussion

4.1. Scatter-to-primary ratio

The non-grid scatter-to-primary ratio was measured three separate times and the average of these measurements was calculated. The non-grid scatter-to-primary ratio measured using the various Solid Water® phantoms and the non-grid imaging condition is shown in figure 1. The SPR values are plotted as a function of projected beam stop radius. For a given beam stop radius, repeat measurements were within 10% of each other. As evident from figure 1, the measured SPR is a function of beam stop size. While not apparent in figure 1, the slope of the data series as a function of beam stop radius is slightly steeper for the thinner phantoms.

To remain consistent with the previous works of other authors (Floyd *et al* 1991) and for the purpose of data presentation, the SPR for a zero beam stop radius (SPR_0) was extrapolated

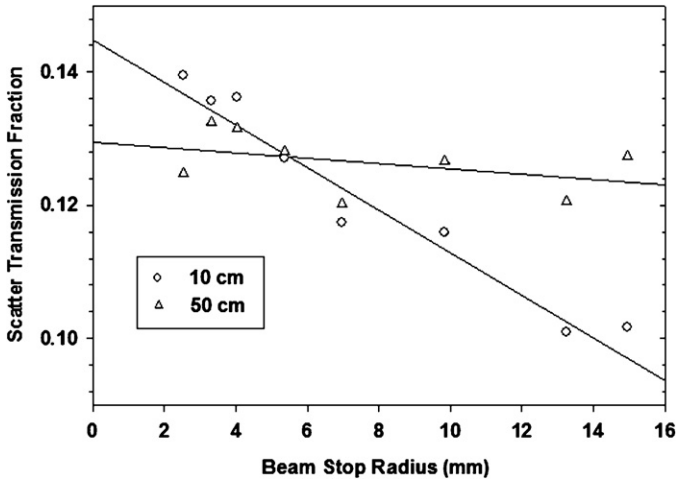

Figure 2. Sample scatter transmission fraction measurements from the N40 r12 grid.

Table 1. Extrapolated non-grid SPR_0 values.

Phantom thickness (cm)	SPR_0
10	2.55
20	5.9
30	10.9
40	17.0
50	25.9

from the measured data. The SPR data were fit to a simple exponential function and the zero radius value of the exponential function was calculated. The discrepancy between the data points of figure 1 and the fit to the data was less than 6%. The extrapolated SPR_0 values were included in figure 1 and are also provided in table 1. The SPR_0 values of table 1 are provided for reference only and were not directly used to measure K_{SNR}. As will be discussed in section 4.4, K_{SNR} was measured independently for each beam stop.

4.2. Scatter transmission

Figure 2 shows the scatter transmission fraction measured for the 10 and 50 cm phantoms as a function of beam stop radius. The data in figure 2 are from the N40 r12 grid. Data from the other grids had different scatter transmission magnitude but was otherwise similar.

As shown in figure 2, and similar to the SPR measurements, the measured scatter transmission fraction was a function of beam stop radius. Also, the rate of change of the scatter transmission as a function of beam stop was dependent upon phantom thickness. The trends of figure 2 are consistent for the various grids used and for repeat experiments. The mechanism behind the changing slope for the different phantom thicknesses is not completely understood. It may be due to differences in the angular distribution of scatter for the various phantom thicknesses. Other authors have demonstrated that scattered radiation contains a strong contribution at shallow scatter angles (5 to 10°) (Muntz *et al* 1983, Chan *et al* 1985). Whether the relative contribution of shallow angle scatter might be affected by phantom thickness is

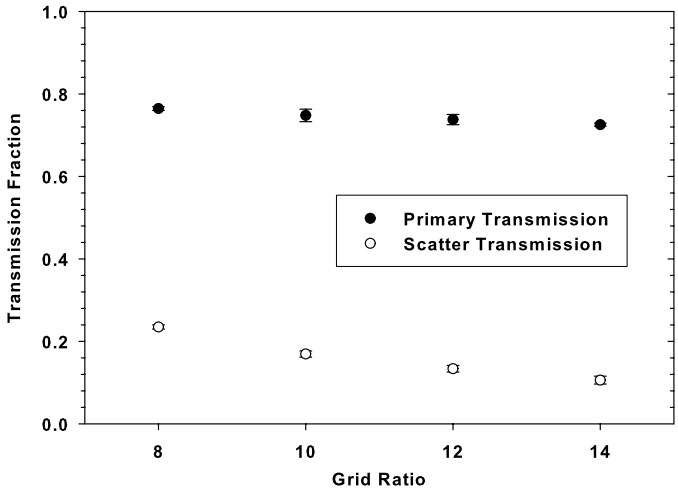

Figure 3. Primary and scatter transmission fraction of the $N = 40\ \mathrm{cm}^{-1}$ grids as a function of grid ratio.

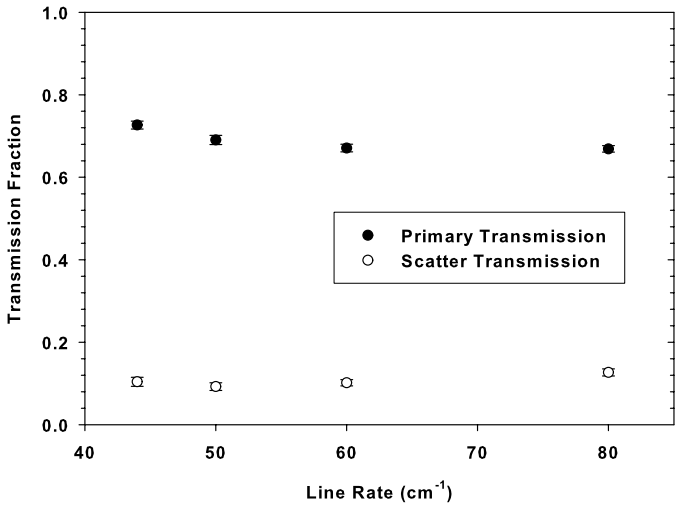

Figure 4. Primary and scatter transmission fraction of the $r = 15{:}1$ grids as a function of line rate.

worth consideration. The mechanism of the change in the slope of the scatter transmission as a function of beam stop radius presents itself as an area of potential future work.

For the purpose of data presentation, the scatter transmission fraction for a zero beam stop radius was extrapolated using a linear fit to the scatter fraction beam stop radii. The average of the extrapolated values was calculated and plotted in figure 3 for the N40 grids and in figure 4 for the r15 grids. The T_S data of figures 3 and 4 include contributions from the various phantom thicknesses. The error bars on the T_S data represent ± 1 standard deviation of the five data points corresponding to the five phantom thicknesses. The T_S data in figures 3 and 4 are provided only for reference and relative comparison. These average values were not used to calculate K_{SNR}. The T_S, T_P and select K_{SNR} data are also provided in table 2.

As shown in figure 3, the scatter transmission fraction of the $N = 40\ \mathrm{cm}^{-1}$ grids decreases with increasing grid ratio. This is because the angular incidence of the scattered x-rays which

Table 2. Scatter and primary transmission factors and SNR improvement factors for the 20 and 50 cm phantoms. The ±1 standard deviation uncertainty in the transmission factors was 0.01 and that of K_{SNR} was less than 0.05.

Grid series		Scatter transmission, T_S	Primary transmission, T_P	K_{SNR} (20 cm phantom, SPR = 5.9)	K_{SNR} (50 cm phantom, SPR = 25.9)
Line rate, $N = 40$ cm^{-1}	$r = 8$:1	0.235	0.764	1.37	1.53
	$r = 10$:1	0.169	0.747	1.49	1.75
	$r = 12$:1	0.134	0.737	1.57	1.89
	r = 14:1	0.106	0.725	1.64	2.07
Grid ratio, $r = 15$:1	$N = 44$ cm^{-1}	0.104	0.727	1.65	2.09
	$N = 50$ cm^{-1}	0.092	0.690	1.63	2.09
	$N = 60$ cm^{-1}	0.102	0.671	1.56	1.95
	$N = 80$ cm^{-1}	0.127	0.669	1.47	1.78

can pass through the grids without striking the lead septa decreases with increasing grid ratio.

Given that the grid ratio of the $r = 15$ grids is fixed, it can generally be expected that, for a given septa thickness, T_S would be independent of line rate. As shown in figure 4, this is generally the case for the 44, 50 and 60 cm^{-1} grids, all of which have 36 μm lead septa. That the scatter transmission of the 80 cm^{-1} grid is higher than the other r15 grids is because it has thinner, 27.5 μm, septa. The thinner septa allow an increase in scatter transmission through the septa.

4.3. Primary transmission

The primary x-ray transmission fraction of the N40 grids is shown in figure 3. The error bars represent the range of three repeat measurements. Given the specified septa thickness (36 μm) and line rate of these grids, the lead septa are expected to occupy 14% of the surface area of the grid. Thus, an ideal grid (without cover or interspace material) is expected to have a primary transmission factor of 0.86. That the primary transmission of the N40 grids is less than the ideal value and decreases with increasing ratio is consistent with attenuation by the front and rear covers and by the fiber interspace material. Considering the four N40 grids, the average primary transmission measured was in the range 85–89% of that expected from an ideal, air interspace grid. That some of the discrepancy between the measured values (0.73 to 0.76) and an ideal transmission factor of 0.86 might be due to imperfections in manufacture and the experimental technique cannot be ruled out. The primary transmission measurements of the N40 grids were an average of 0.016 (range 0.012 to 0.022) less than that specified by the grid manufacturer. That the results of this work and the data provided by the manufacturer are similar provides mutual support that both are reasonable measurements.

The primary x-ray transmission fraction of the r15 grids is shown in figure 4. The changes in the primary x-ray transmission as a function of line rate are consistent with changes in the relative surface area of these grids that is occupied by the lead septa. For a fixed septa thickness (36 μm), the relative surface area of the grids increases, thereby decreasing primary x-ray transmission. The relative change in T_P for the 44, 50 and 60 cm^{-1} grids is consistent with this argument. The 80 cm^{-1} grid has thinner lead septa (27 μm), and T_P for this grid is consistent with that expected given the line rate and septa thickness. Considering the four r15 grids, the average primary transmission measured was in the range of 84–86% of that expected from an ideal, air interspace grid. The primary transmission measurements of the r15 grids were an average of 0.021 (range 0.013 to 0.029) less than that specified by the grid manufacturer.

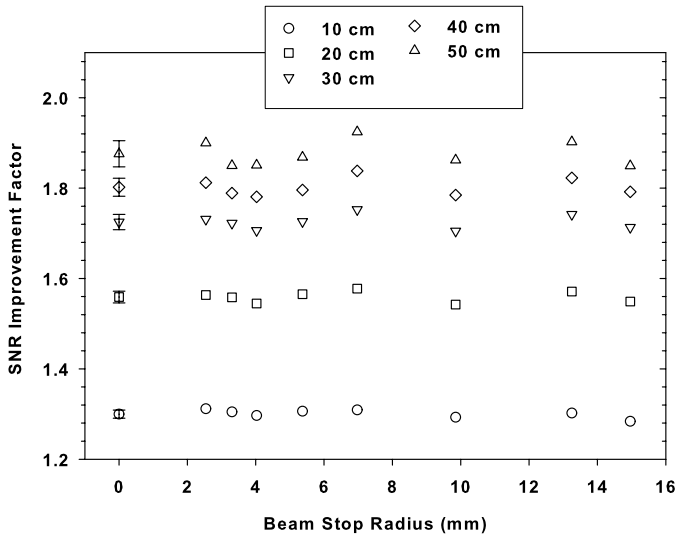

Figure 5. SNR improvement factor for the N40 r14 grid for various phantom thicknesses and plotted versus beam stop radius.

4.4. SNR improvement factor

The SNR improvement factor was calculated for each phantom thickness, grid and beam stop radius using equation (1). Representative K_{SNR} for the N40 r12 grid is shown in figure 5. K_{SNR} increases as a function of phantom thickness because the thicker phantoms result in higher SPR, thereby providing greater opportunity for the grids to improve SNR by removing scattered x-rays. K_{SNR} was found to be independent of the beam stop radius; therefore, the average of the measurements from the eight beam stops was calculated. The average K_{SNR} for the N40 r12 grid is shown in figure 5 as the zero beam stop radius data point. There is systematic variation in the K_{SNR} data of figure 5 that is correlated with the beam stop radius. These data inherited this variation from the non-grid SPR data shown in figure 1, which were acquired using a single storage phosphor. This error is attributable to a systematic variation in the response of the detector over the imaging area (detector non-uniformity). The error bars on the zero radius point represent ± 1 standard deviation of the individual beam stop K_{SNR} values. Note that K_{SNR} was the same when it was calculated using the extrapolated SPR and T_P data rather than the individual beam stop data. Sample K_{SNR} data for the various grids and the 20 and 50 cm phantoms is provided in table 2.

The SNR improvement factor of the $N = 40$ cm^{-1} grids is shown in figure 6. The data in figure 6 were measured using phantom thicknesses in the range of 10–50 cm, whereas the data are plotted versus the corresponding SPR_0 provided in table 1. The error bars in figure 6 represent ± 1 standard deviation of K_{SNR} of the eight beam stops. For the N40 grids, K_{SNR} increased with increasing grid ratio. This is the expected result as the primary transmission is relatively invariant with grid ratio whereas the scatter transmission decreased substantially with increasing grid ratio (figure 3). Over the range of phantom thicknesses and corresponding SPRs encountered in this work, the preferential ordering of the grids is independent of the magnitude of the non-grid SPR. That is, the best performing grid was the same under all scatter conditions.

Under a zero scatter condition, the SNR improvement factor is expected to be equal to the square root of the primary transmission factor. K_{SNR} under this zero scatter condition is

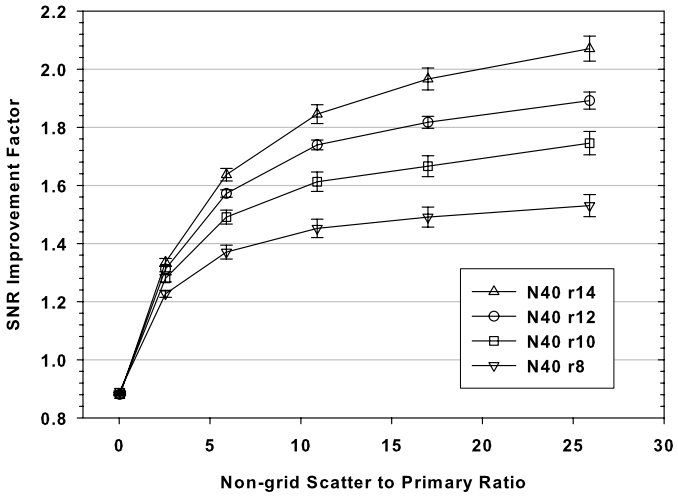

Figure 6. SNR improvement factors for the fixed line rate ($N = 40$ cm^{-1}) grids, plotted as a function of the extrapolated zero beam stop SPR_0 values. The SPR values correspond to the various phantom thicknesses in the range from 0 (Bucky only) to 50 cm.

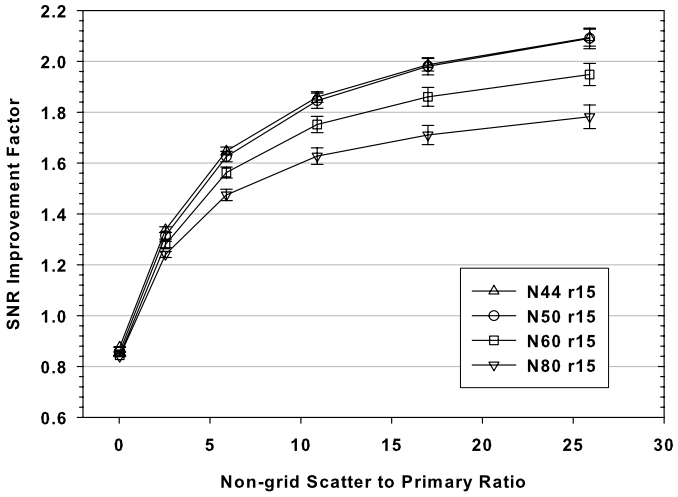

Figure 7. SNR improvement factors for the fixed ratio ($r = 15{:}1$) grids, plotted as a function of the extrapolated zero beam stop SPR_0 values.

also shown in figure 6. K_{SNR} values greater than 1 indicate a net SNR benefit from grid use, and values less than 1 indicate a net detriment to the SNR. The data of figure 6 suggest that these grids would demonstrate modest image quality detriment for imaging conditions where the SPR is less than approximately 1.0.

The average SNR improvement factor of the r15 grids is plotted in figure 7 versus the extrapolated SPR_0 values. The error bars in figure 7 represent ± 1 standard deviation of the eight beam stop radius measurements. Overall, the SNR improvement factor showed a trend of decreasing performance as the line rate was increased from 44 to 80 cm^{-1}. The N44 and N50 grids have average K_{SNR} values that are, essentially, equivalent. The K_{SNR} value of the

N60 grid was reduced by 7% as compared to these two grids, and that of the N80 grid was reduced by 11%. The N80 grid performance is compromised by a modestly reduced primary transmission factor and a scatter transmission factor that exceeds that of the remaining r15 grids by an average of nearly 30%. The increased scatter transmission may be due to increased scatter x-ray penetration through the thinner lead septa of this grid (27 versus 36 μm). Whereas it might be expected that the lowest line rate ($N = 44$ cm^{-1}) grid may be preferable due to increased primary transmission (figure 4), the experimental K_{SNR} data did not support this hypothesis. The mechanism of the (unexpected) similarity between the N44 r15 and N50 r15 grids is unknown.

5. General discussion

Because it was readily available, a computed radiography system was used to measure grid performance. The non-grid SPR reported in figure 1 and used to calculate K_{SNR} via equation (1) is specific to this modality. However, the scatter and primary transmission of the grids is independent of the imaging modality. Therefore, the transmission values reported here can be used to predict K_{SNR} for these grids used with another digital imaging system, provided that the non-grid SPR of that system is known.

Given the non-grid SPRs encountered in this work, all of the grids demonstrated the potential to improve image quality compared to a non-grid technique. For the 20 cm phantom, the SNR improvement factor ranged from 1.37 to 1.65. The N40 r14, N44 r15 and N50 r15 grids had K_{SNR} values which were within 1% of one another and they were the three best performing grids studied. The non-grid SPR_0 for the 20 cm thick phantom was 5.9. For this phantom, the SNR improvement factor for the best performing grids was, on average, 1.64. The image quality improvement that might be expected by using this grid versus the non-grid technique is equivalent to increasing the current–time (mA s) technique of the non-grid condition by a factor $1.64^2 = 2.7$. Considering the high SPR associated with the 50 cm phantom, use of the optimal grids provided a quantum noise improvement that is consistent with a current–time technique increase by a factor of $2.09^2 = 4.4$. Use of the highest line rate (80 cm^{-1}) r15 grid rather than the lower line rate (N44 and N50) r15 grids resulted in an overall quantum efficiency loss of 27% for the 50 cm phantom.

Figure 6 showed a steady K_{SNR} improvement with increasing grid ratio for a fixed line rate (40 cm^{-1}). This trend suggests that a further increase in grid ratio may result in a grid with improved K_{SNR}. However, higher ratio grids are more susceptible to primary x-ray attenuation caused by the interspace material and misalignment, including linear Bucky motion, and there is a (unknown) practical upper limit to grid ratio.

The experiments described herein were designed to evaluate grid performance under well-controlled circumstances. Care was taken to ensure proper focus distance and alignment. This work supports the use of high ratio grids with digital imaging systems in which the x-ray imaging geometry can be made to match the grid specifications (or vice versa). The influence of improper focal distance (Boldingh 1962) and angular alignment with the primary x-ray beam (Carlin *et al* 1996) have been presented by others. It is important to note that even the relatively modest misalignment ($\pm$1.3 cm) attributable to typical linear Bucky motion contributes to additional primary x-ray attenuation, the influence of which increases with increasing grid ratio. Preliminary measurements suggest that, for the grids studied in this work, preferential ordering will not be affected by the influence of linear Bucky motion. Misalignment of the grids due to Bucky motion may be minimized by decreasing the range of linear motion of the grids.

The primary x-ray transmission was measured using the unfiltered (by phantom material) 104 kVp beam produced by the x-ray tube. This standard clinical tube used for this experiment had additional aluminum filtration such that the half value layer of an 80 kVp beam was 3.5 mm Al. It is reasonable to expect that T_P would be a function of beam quality and, therefore, might vary with changes in kVp and patient or phantom thickness. A simple experiment was conducted to estimate the error in these results attributable to use of an unfiltered beam to measure the primary transmission. Using x-ray beam spectral modeling, the half value layer of the primary spectrum exiting the 50 cm phantom was estimated to be 11 mm Al. Modeling demonstrated that an equivalent half value layer could be achieved using 4.9 cm Al rather than 50 cm Solid Water®. The primary transmission of the N44 r15 grid (3 mm tall) was measured using the 104 kVp beam filtered by various thicknesses of Al in the range of 0–5 cm. To minimize the influence of scatter from the Al attenuator, the Al was placed as close as possible to the x-ray source and narrow beam geometry was used. The primary transmission through the N44 r15 grid was found to increase by 0.03 as the Al filtration was increased from 0 to 5 cm Al. Given the beam qualities and grids used in this experiment, this is a 'worst case' bias error estimate associated with the use of the unfiltered 104 kVp to measure primary x-ray beam transmission. Propagation of this error through equation (1) suggests that the SNR improvement factor reported in this work may be understated by as much as 3.5%. The influence of this error is expected to decrease for phantoms thinner than 50 cm and grids that are shorter than 3 mm. It is important to note that the influence of beam quality on primary x-ray transmission would be substantially greater if a lower peak tube potential or grids with a different interspace material had been used. Specifically, it can be anticipated that use of aluminum for an interspace material would contribute to increased attenuation of the primary x-ray fluence, thereby decreasing the overall performance of such a grid (McDaniel *et al* 1984, Sandborg *et al* 1994).

The experimental method of this work included a fixed $30 \times 30\ \text{cm}^2$ field of view, phantom thicknesses in the range 10 to 50 cm and a peak tube potential of 104 kVp. The field of view is consistent with that suggested by IEC 60627. The thickness range was selected to mimic a large range of clinically relevant thicknesses, and the kVp was consistent with that used for imaging large patient anatomy. While the use of this high kVp for thin body parts (and phantoms) is not clinically appropriate, 104 kVp was used for all phantom thicknesses to provide consistency. Overall, this study was set up to investigate grid use for large body parts that have a correspondingly high SPR. Measurements performed by (and readily available from) the manufacturer per the recommendations provided by IEC 60627 (20 cm phantom, 80 kVp) demonstrated similar trends for grid performance. Specifically, the preferential ordering of the grids identified in this study using 104 kVp was consistent with that found using 80 kVp. Of course, small body parts are often thinner and have less volume and have correspondingly lower SPR. They would also be imaged with a lower kVp than used in this work. Use of a lower kVp is expected to result in decreased primary transmission due to increased attenuation by the interspace material. Given this, a study to specifically investigate optimum grid (or non-grid) use for small pediatric and neo-natal patients using lower kVps may prove to be useful.

While the magnitude of the SNR improvement factor was a function of phantom thickness and the corresponding SPR, selection of the optimum grid was independent of phantom thickness. Per equation (1), if it can be assumed that the primary and scatter transmission fractions are (reasonably) independent of phantom thickness, then these parameters can be measured for a single phantom thickness and used to predict the SNR improvement factor for any SPR condition. The IEC 60627 suggests that measurements can be acquired using a 20 cm thick water phantom. This current work does not provide evidence to suggest that a different

standard phantom thickness should be used. It should be noted, however, that the specification of K_{SNR} under only this single, relatively low SPR condition, substantially underestimates the potential usefulness of a grid for very high scatter imaging conditions.

As was shown in the work of previous investigators (Floyd *et al* 1991), the scatter-to-primary ratio measured using a graduated beam stop method is a function of the beam stop radius. Not coincidently, this work also showed that the scatter transmission fraction of a grid is also a function of beam stop radius. This work demonstrated that the mathematical combination of these two factors into the SNR improvement factor results in K_{SNR} values which are independent of beam stop radius. Given this, it is reasonable to conclude that the SNR improvement factor of a grid could be measured using a single beam stop radius. While strictly true, the authors feel that a graduated beam stop method is still relevant. The graduated beam stop method provides data such that a zero beam stop radius SPR, and T_S values can be calculated and provides SPR_0 that may be compared to other published data.

A recent review of commercially available digital radiography imaging devices showed that there is a wide range of grids used by these devices. The line rate of the available grids ranged from 40 to 80 cm^{-1} and the ratio ranged from 4:1 to 12:1. Some of the grids had aluminum interspace material and others had a fiber interspace material. Some of the grids were used in a moving Bucky type mechanism and some were held stationary. Given the large range of grids available, it seems unlikely that the grid(s) for each system was selected based on its ability to provide optimum image quality. In general, the grids that were stationary had a relatively high line rate. The high line rate serves to minimize the potential for image artifacts caused by the discrete sampling of the grid by the digital detector. It has been the experience of the authors that the use of grids with low line rates (40 to 50 cm^{-1}) in digital systems that have relatively high spatial blur (some computed radiography) does not result in image artifacts due to grid sampling. In this case, the imaging detector tends to blur the gridlines enough to make them irrelevant. For any clinical implementation of stationary grids, a preliminary investigation of the potential to create grid artifacts is warranted. Some of the systems with stationary grids were portable and it is reasonable that a moving grid mechanism would be prohibitively large and bulky. In other systems, stationary grids were implemented in x-ray tables and wall stands. For a given grid ratio and septa thickness, the potential for image quality improvement decreases with increasing line rate. To help ensure the best image quality, high line rate grids should be avoided except in circumstances where a stationary grid is used with a high-resolution imaging detector. It is worth noting that, even when grid artifacts are present in images, there is a potential to remove them with image processing (Belykh and Cornelius 2001, Barski and Wang 1999).

6. Conclusions

Proper antiscatter grid use is important to assure optimum image quality with digital x-ray imaging systems. This is especially true for large patient anatomy with inherently high scatter-to-primary ratio. Of the grids tested here, the N40 r14, N44 r15 and N50 r15 grids had the highest SNR improvement factor when used with a computed radiography system. The primary and scatter transmission fractions herein could be used to predict K_{SNR} for any digital imaging system, provided that the non-grid SPR associated with that system is known. The results of this work can be used to guide both manufacturing development and clinical implementation of digital x-ray imaging systems which are optimized for overall efficiency and image quality. The authors are hopeful that even better grids will be created in the future.

Appendix

The signal-to-noise ratio improvement factor is the ratio of the quantum SNR of an image acquired using a grid (SNR_G) versus that acquired using a non-grid technique (SNR). For the purposes of this work, it is appropriate to define the SNR in terms of the net image signal contribution attributable to the detected primary x-ray fluence (S_P), the scattered x-ray fluence (S_S) and the relative attenuation (k) of the primary x-ray beam by an object embedded in a uniform scattering medium. The quantum SNR of the object using the non-grid technique is

$$\mathrm{SNR} = \frac{kS_P}{(S_P + S_S)^{0.5}}. \tag{A.1}$$

Given that the scatter-to-primary ratio of the non-grid technique is defined by

$$\mathrm{SPR} = \frac{S_S}{S_P}, \tag{A.2}$$

the SNR of the non-grid technique can be rewritten as

$$\mathrm{SNR} = \frac{kS_P}{(S_P(1 + \mathrm{SPR}))^{0.5}}. \tag{A.3}$$

Similarly, the SNR of the grid technique can be defined as

$$\mathrm{SNR_G} = \frac{kT_PS_P}{(T_PS_P + T_SS_S)^{0.5}}, \tag{A.4}$$

where T_P and T_S are the fractions of primary and scatter x-rays, respectively, transmitted by the grid. Equation (A.4) can be rearranged to

$$\mathrm{SNR_G} = \frac{kT_PS_P}{(T_PS_P(1 + \mathrm{SPR_G}))^{0.5}}. \tag{A.5}$$

The SNR improvement factor is the ratio of the SNR of the grid technique to that of the non-grid technique;

$$K_{\mathrm{SNR}} = \frac{\frac{kT_PS_p}{(T_PS_P(1+\mathrm{SPR_G}))^{0.5}}}{\frac{kS_p}{(S_P(1+\mathrm{SPR}))^{0.5}}}, \tag{A.6}$$

which simplifies to

$$K_{\mathrm{SNR}} = \frac{T_P^{0.5}(1 + \mathrm{SPR})^{0.5}}{(1 + \mathrm{SPR_G})^{0.5}}. \tag{A.7}$$

Substitution of

$$\mathrm{SPR_G} = \frac{T_S}{T_P}\mathrm{SPR} \tag{A.8}$$

into equation (A.7) results in the SNR improvement factor as a function of the primary and scattered x-ray transmission factors of the grid as well as the SPR of the non-grid condition,

$$K_{\mathrm{SNR}} = \frac{(1 + \mathrm{SPR})^{0.5}T_P}{(T_P + T_S\mathrm{SPR})^{0.5}}. \tag{A.9}$$

Because antiscatter grid studies have historically reported the contrast improvement factor (or independent SPR and SPR_G) and the Bucky factor of the grid techniques used, a definition of K_{SNR} using these terms was desired. The Bucky factor is defined as

$$B = \frac{S_P + S_S}{T_PS_P + T_SS_S}, \tag{A.10}$$

which can be rewritten as

$$B = \frac{(1 + \mathrm{SPR})}{T_\mathrm{P}(1 + \mathrm{SPR_G})}. \tag{A.11}$$

Solving the definition of the Bucky factor (equation (A.11)) for T_P and calculating the square root of that definition results in

$$T_\mathrm{P}^{0.5} = \frac{(1 + \mathrm{SPR})^{0.5}}{B^{0.5}(1 + \mathrm{SPR_G})^{0.5}}. \tag{A.12}$$

Substituting equation (A.12) into equation (A.7) results in

$$K_\mathrm{SNR} = \frac{(1 + \mathrm{SPR})}{B^{0.5}(1 + \mathrm{SPR_G})}. \tag{A.13}$$

Substituting the definition of the contrast improvement factor (K_C),

$$K_\mathrm{C} = \frac{(1 + \mathrm{SPR})}{(1 + \mathrm{SPR_G})}, \tag{A.14}$$

into equation (A.13) results in

$$K_\mathrm{SNR} = \frac{K_\mathrm{C}}{B^{0.5}}. \tag{A.15}$$

The alternative definitions of K_SNR presented here provide a means to predict grid performance in a digital imaging system from historical measurements based on screen–film systems.

References

Barski L and Wang X 1999 Characterization, detection, and suppression of stationary grids in digital projection radiography imagery *Image Display; Proc. SPIE* **3658** 502–19

Belykh I and Cornelius C W 2001 Antiscatter stationary-grid artifacts automated detection and removal in projection radiography *Image Process.; Proc. SPIE* **4322** 1162–6

Boldingh W H 1962 Quality and choice of Potter Bucky grids: Parts IV and V *Acta Radiol.* **55** 225–35

Bonenkamp J G and Boldingh W H 1959a Quality and choice of Potter Bucky grids: I. A new method for the unambiguous determination of the quality of a grid *Acta Radiol.* **51** 479–89

Bonenkamp J G and Boldingh W H 1959b Quality and choice of Potter Bucky grids: II. Application of the criterion of quality to various types of signals *Acta Radiol.* **51** 149–57

Bonenkamp J G and Boldingh W H 1959c Quality and choice of Potter Bucky grids: III. The choice of a Bucky grid *Acta. Radiol.* **52** 241–53

Bucky G 1913 Über die ausschaltung de rim objekt entstehenden sekundär-strahlen bei röntgenanfnahmen *Verh. Dsch. Ront. Ges.* **9** 30

Carlin M D, Nishikawa R M, MacMahon H and Doi K 1996 The effect of x-ray beam alignment on the performance of antiscatter grids *Med. Phys.* **23** 1347–50

Chan H-P, Higashida Y and Doi K 1985 Performance of antiscatter grids in diagnostic radiology: experimental measurements and Monte Carlo simulation studies *Med. Phys.* **12** 449–54

Chan H-P, Lam K L and Wu Y 1990 Studies of performance of antiscatter grids in digital radiography: effect on signal-to-noise ratio *Med. Phys.* **17** 655–64

Chen C-W, Taylor K W and Holloway A F 1995 The spectrum and angular distribution of x rays scattered from a water phantom *Med. Phys.* **22** 1235–45

Dick C I and Motz J W 1978 New method for the experimental evaluation of x-ray grids *Med. Phys.* **5** 133–40

Doi K, Frand P H, Chan H-P, Vyborny C J, Makino S, Iida N and Carlin M 1983 Physical and clinical evaluation of new high-strip-density radiographic grids *Radiology* **147** 575–82

Fetterly K A and Hangiandreou N J 2001 Effects of x-ray spectra on the DQE of a computed radiography system *Med. Phys.* **28** 241–9

Floyd C E, Lo Y, Chotas H G and Ravin C E 1991 Quantitative scatter measurement in digital radiography using a photostimulable phosphor imaging system *Med. Phys.* **18** 408–13

Flynn M J and Samei E 1999 Experimental comparison of noise and resolution for 2k and 4k storage phosphor radiography systems *Med. Phys.* **26** 1612–23

IEC 2001 Diagnostic x-ray imaging equipment—characteristics of general purpose and mammographic anti-scatter grids *IEC International Standard* 60627 (Geneva: International Electrotechnical Commission)

Kalender W A 1982 Calculation of x-ray grid characteristics by Monte Carlo methods *Phys. Med. Biol.* **27** 353–61

McDaniel D L, Cohen G, Wagner L K and Robison L H 1984 Relative dose efficiencies of antiscatter grids and air gaps in pediatric radiography *Med. Phys.* **11** 508–12

Morgan R H 1946 An analysis of the physical factors controlling the diagnostic quality of Roentgen images: Part III. Contrast and the intensity distribution function of Roentgen images *Am. J. Roent.* **55** 67–89

Motz J W and Danos M 1978 Image information content and patient exposure *Med. Phys.* **5** 8–22

Muntz E P, Fewell T, Jennings R and Bernstein H 1983 On the significance of very small angle scattered radiation to radiographic images at low energies *Med. Phys.* **10** 819–23

Neitzel U 1992 Grids and air gaps for scatter reduction in digital radiography: a model calculation *Med. Phys.* **19** 475–81

Sandborg M, Dance D R, Persliden J and Alm Carlsson G 1994 A Monte Carlo program for the calculation of contrast, noise, and absorbed dose in diagnostic radiology *Comput. Methods Prog. Biomed.* **42** 167–80

Tucker D M, Souto M and Barnes G T 1993 Scatter in computed radiography *Radiology* **188** 271–4

Wagner R F 1977 Noise equivalent parameters in general medical radiography: the present picture and future picture *Photo. Sci. Eng.* **21** 252–61

Wagner R F, Barnes G T and Askins B S 1980 Effect of reduced scatter on radiographic information content and patient exposure: a quantitative demonstration *Med. Phys.* **7** 13–8

Wilsey R B 1921 The intensity of scattered x-rays in radiography *Am. J. Roent.* **8** 328–39

Yip K L, Whiting B R, Kocher T E, Trauernicht D P and Van Metter R L 1996 Understanding the relative sensitivity of radiographic screens to scattered radiation *Med. Phys.* **23** 1727–37